Research article

Strain induced structural phase transition and compositional dependent magnetic phase transition in Ti doped $Bi_{0.80}Ba_{0.20}FeO_3$ ceramics

Shohel Rana [a], Syeda Karimunnesa [b], F. Alam [c], Bablu Chandra Das [a,c,*], F.A. Khan [a]

[a] Department of Physics, Bangladesh University of Engineering and Technology, Dhaka, 1000, Bangladesh
[b] Department of Physics, University of Chittagong, Chittagong, 4331, Bangladesh
[c] Department of Physical Sciences, Independent University, Dhaka, 1229, Bangladesh

A B S T R A C T

$Bi_{0.80}Ba_{0.20}Fe_{1-x}Ti_xO_3$ ($0 \leq x \leq 0.10$) samples are prepared using solid state reaction technique. Bi^{3+} site is replaced with 20 % Ba^{2+} which induced structural modification from rhombohedral to pseudo cubic accompanied by the creation of oxygen vacancies owing to the charge reimbursement. Fe^{3+} site is replaced with different concentrations of Ti^{4+} keeping Ba content fixed. All the samples exhibited similar morphology and no significant variation in grain size is observed by substituting Ti at Fe site. All of the samples exhibited ferromagnetic behavior, which is ascribed to the destruction of spiral spin structures and changes in super-exchange interaction strength caused by variations in bond lengths of Fe–O and Fe–O–Fe. The decrease in magnetization with increasing Ti concentration is due to magnetic moment dilution caused by non-magnetic Ti^{4+}. An anomalous trend in magnetization is observed for magnetic measurements at low temperature (77 K) where structural transformation from ferromagnetic to diamagnetic behavior was noted for 10% Ti content. Further, because of the incorporation of Ti^{4+}, an improved dielectric property was observed due to increase in resistivity and decrease in the defect concentration (oxygen vacancies). In the present study, it was concluded that optimum concentration of Ba^{2+} (20%) and Ti^{4+} co-doped $BiFeO_3$ systems have shown enhanced multiferroic properties at room temperature.

1. Introduction

Multiferroic materials have received much more attention in the modern world for potential applications in the digital era for data storage devices, i.e. Photovoltaic cells and magnetoelectric memories and sensors etc. [1, 2, 3, 4]. Multiferroic materials possess more than one primary ferroic property [5, 6], i.e. (anti) ferroelectricity and (anti) ferromagnetism. Unfortunately, very rare in nature due to the requirement of empty d^0 orbitals for ferroelectricity and partially filled d orbitals for ferromagnetism [7]. However, with this coexistence, there is possibility that magnetization and polarization can be tuned by electric and magnetic field which is termed as magnetoelectric (ME) effect [8]. In this regard, Bismuth ferrite, $BiFeO_3$ (BFO) has become a potential candidate due to its novel properties and immense applications [9, 10]. BFO is a fascinating multifunctional material with unique physical properties [11, 12, 13, 14, 15]. In addition to this, BFO is a rare sole phase room temperature multiferroics which shows promising application due to high ferroelectric and antiferromagnetic transition temperature ($T_c \sim 1103\,K$,

$T_N \sim 643\,K$) [16]. The rhombohedral structure of pure BFO has an *R3c* space group with antiferromagnetic spin structure along with incommensurate long range ($\lambda = 62\,nm$) cycloidal spin structure [17]. The Dzyaloshinsky-Moriya (DM) interaction influences long-range G-type antiferromagnetic ordering [18].

BFO, as a multifunctional electromagnetic material, has piqued the interest of many researchers [19]. Its microstructure has been extensively studied in terms of its effect on electromagnetic and multiferroic properties [20, 21, 22]. By suppressing oxygen vacancies and the valence effect, (Nd/V) co-doped BFO shows enhanced photovoltaic and ferroelectric properties [23]. Li substituting in BFO causes phase separation, resulting in a BFO - spinel $LiFe_5O_8$ nanocomposite with room temperature magnetic behavior from $LiFe_5O_8$ [24]. The Sm/Nb co-substituting changes the space group of BFO, which appears to improve its multiferroic properties [25]. Due to changes in lattice anisotropy, Nb ions can tune the domain configurations in BFO thin films [26]. Owing to polarization flipping at the $Pt/(Bi_{0.9}Sm_{0.1})$ $(Fe_{0.97}Hf_{0.03})O_3$ interface, $Pt/(Bi_{0.9}Sm_{0.1})$ $(Fe_{0.97}Hf_{0.03})O_3/LaNiO_3$ heterostructures have improved

---

* Corresponding author.

E-mail addresses: bcdasbuetsets@iub.edu.bd, bcdasbuet@gmail.com (B. Chandra Das).

photovoltaic properties [27]. BFO has electromagnetic absorption performance due to its multiferroic properties, but it is limited.

Instead of numerous interesting features, BFO has several drawbacks like presence of secondary phases, high leakage current, high dielectric loss, and weak ME coupling which limit its practical application [28]. In order to overcome these issues, several attempt have been made to replace A-site Bi^{3+} and B-site Fe^{3+} site ions with dopants such as Ba^{2+} [29], Sr^{2+} [30], Ca^{2+} [31], La^{3+} [32], Gd^{3+} [33] and Ti^{4+} [34], Mn^{4+} [35], Nb^{5+} [36] to enhance the ferroelectric and ferromagnetic properties, respectively. Among various kinds of doping at A-site, 20% Ba doping showed enhanced magnetization by improving the phase purity of BFO [37]. On the other hand, partial replacement of Fe^{3+} by non-magnetic Ti^{4+} can reduce the leakage current with the removal of oxygen vacancies [38, 39]. Besides, the dielectric of BFO and doped BFO shows featured frequency response in microwave field because of its defect and distorted structure [40]. The amount of doping has an effect on both magnetic and dielectric properties. These are beneficial to tuning microwave absorption of BFO [11]. In this study, we want to improve the dielectric and magnetic characteristics of BFO by replacing A-site Bi^{3+} by Ba^{2+} and B-site Fe^{3+} by Ti^{4+} ions. Ba^{2+} substitution at Bi^{3+} will induce oxygen vacancies or can change the valence from Fe^{3+} to Fe^{2+} due to charge compensation [41]. Secondly, the substitution of Ba^{2+} which has large ionic radii (1.42 Å) as compared to Bi^{3+} (1.17 Å) can induce lattice strains [34, 37]. Consequently, charge imbalance and induced strain suppressed the spiral spin structure, releasing the spiral's locked magnetization [42]. The suppression of spiral is usually achieved due to the structural transformation (Breaking/weakening or R3c symmetry). Mahbub et al. [43] reported that 20% Ba doping in BFO transformed structure to tetragonal while Rout et al. [44] reported that both *R3c* and *P4mn* space group coexist. Further, Shahzad et al. [35, 37] reported that 20% Ba doping in A site of BFO can suppress secondary phases and significantly enhances the magnetic properties of the system by suppressing the spiral spin structure. Thus, Ba^{2+} substitution can be beneficial to induce and enhance magnetization in BFO. However, the generation of oxygen vacancies on the other hand can hamper the dielectric and ferroelectric properties due to leakage current [37]. This issue can be resolved by co-substitution at Fe^{3+} site with ions of higher valence state. As Ti and Fe ions exist in +4 and +3 states, the substitution of Ti will compensate the loss of positive charge due to substitution of Ba^{+2} with Bi^{3+} site. Such substitution resulted a reduce in the concentration of oxygen vacancies by charge compensation mechanism. Moreover, Ti^{4+} substitution will improve the resistivity of the prepared systems.

Herein, the idea is to replace Bi^{3+} by Ba^{2+} (at Bi site, 20% Ba is fixed) and changing the Fe^{3+} content by Ti^{4+}. Local structural, magnetic, and dielectric properties of $Bi_{0.80}Ba_{0.20}Fe_{1-x}Ti_xO_3$ ($0 \leq x \leq 0.10$) system were investigated. The properties of these systems have been explained considering the effects of composition, differences in size and electronic configuration between the host elements (Bi, Fe) and the substituents (Ba, Ti). These optimized systems are expected to have very good magnetic as well as electrical properties. To the best of our knowledge, there have been no studies of Ti^{4+} -substituted $Bi_{0.80}Ba_{0.20}FeO_3$ prepared by solid-state reaction method.

2. Experimental details

The $Bi_{0.80}Ba_{0.20}FeO_3$ (BBFO), $Bi_{0.80}Ba_{0.20}Fe_{0.98}Ti_{0.02}O_3$ (BBFTO1), $Bi_{0.80}Ba_{0.20}Fe_{0.94}Ti_{0.06}O_3$ (BBFTO2), and $Bi_{0.80}Ba_{0.20}Fe_{0.90}Ti_{0.10}O_3$ (BBFTO3) compositions were synthesized using a planetary ball milling and a solid state reaction method. High purity oxides like Bi_2O_3, $BaCO_3$, TiO_2 and Fe_2O_3, were carefully weighted according to their stoichiometric ratio extracted after balancing chemical equations. To homogenize the powder, the weighed samples were grinded in a mortar for 1 h and 30 min and then ball milled further for about 6 h. The ball milled samples were then calcined at 1123 K for 30 min followed by an intermediate grinding. The samples were then palletized using hand presser under 500 psi where PVA (polyvinyl alcohol) was used as a binder. The palletized samples were sintered at 1123 K for 30 min. We adopted identical heat treatment temperature to compare changes in the properties. The X-ray diffraction (XRD) data was recorded in the range $0^0 \leq 2\theta \leq 80^0$ using PANalytical EMPERION diffractometer with CuK_α ($\lambda = 1.540598$ Å) radiation in continuous scanning mode. Structural refinement has been performed with the GSAS software by employing the Rietveld refinement technique. After refinement, CIF files were extracted, and structure was visualized using VESTA program where bond length and bond angles were calculated. A field emission scanning electron microscope (FE-SEM; JSM 7600F, JEOL-Japan) was used to examine the surface morphology and microstructure of the samples. For the magnetization measurement, we have used vibrating sample magnetometer (VSM). A pure Ni usual sample was used to calibrate the instrument. In fields between $-1 T \leq 0 \leq 1T$, the M vs. H hysteresis loops were recorded at 298 K and 77 K. To measure dielectric properties, all of the pellets were polished and converted to parallel plate capacitors by introducing silver paste on opposite faces of the pellets. The pellets were dried at 373 K for 2 h before taking the room temperature and temperature dependent dielectric data using precision impedance analyzer (Model: Wayne Kerr 6500B).

3. Result and discussion

3.1. Structural properties

The crystallographic structures of BBFO, BBFTO1, BBFTO2, and BBFTO3 samples were examined by XRD. Figure 1(a) shows the complete XRD patterns and Figure 1(b) shows the enlarged view of XRD patterns from 31° to 33° of pristine BFO, BBFO, BBFTO1, BBFTO2, BBFTO3 ceramics at room temperature. Figure 2a, b, c, d show the Rietveld fitted XRD patterns and values of crystal structure parameters extracted after fitting are summarized in Table 1. Rietveld analysis suggests that BFO crystalized in rhombohedral *R3c* structure whereas BBFO sample crystallized in both rhombohedral *R3c* and pseudo cubic *Pm$\bar{3}$m* structures. Both these samples contained slight amount of Bi^{3+} rich impurity phase ($Bi_{25}FeO_{40}$). This impurity phase has been usually reported [45]. Other Ti^{4+} substituted samples were carefully checked for secondary phases using qualitative Rietveld refinement technique (Figure 2), but no impurity peaks were observed. The absence of impurity peaks for BBFTO1, BBFTO2, and BBFO3 samples indicate that impurity phases were not formed as a result of Ti^{4+} substitution and stabilize the structure. Moreover, XRD exploration suggest that doubly split peaks observed for pure BFO around 32° corresponding to (104) and (110) planes, around 37° corresponding to (006) and (202) planes, around 52° corresponding to (211) and (116) planes, and around 58°; corresponding to (018) and (214) planes eventually to form single broad peak on addition of 20% Ba^{2+} substitution at Bi^{3+} site. Figure 1(b) shows one of these four doubly split peaks which merged together to form a single broad peak. This merging of two peaks into one broad peak indicates a structural phase transformation from *R3c* (rhombohedral) to *Pm$\bar{3}$m* (pseudo cubic) symmetry. Rietveld refinement confirmed that rhombohedral *R3c* symmetry is changing to pseudo cubic *Pm$\bar{3}$m*. Whereas the shift in 2θ peak for BBFO sample towards the lower angles indicates increase in unit cell volume which occurred due to size difference between Ba^{2+} (1.42 Å) and Bi^{3+} (1.03 Å) ions. We also noted that with inclusion of Ti^{4+} ions (BBFTO1, BBFTO2, and BBFTO3 samples) a slight shift of diffraction peaks towards the lower angles has been observed which indicates slight increase in lattice parameter and is attributed to the ion size difference between Fe^{3+} (0.64 Å) and Ti^{4+} (0.68 Å). Ti^{4+} found at grain boundaries may be responsible for the increase in lattice parameter [46]. However, no differences occurred with peak shapes after Ti^{4+} incorporation indicating that structure transformation is same as that of the BBFO sample. Makhdoom et al. [47] reported similar structural transformation on 10% Ba doped BFO system. Similar kinds of structural transformation has also
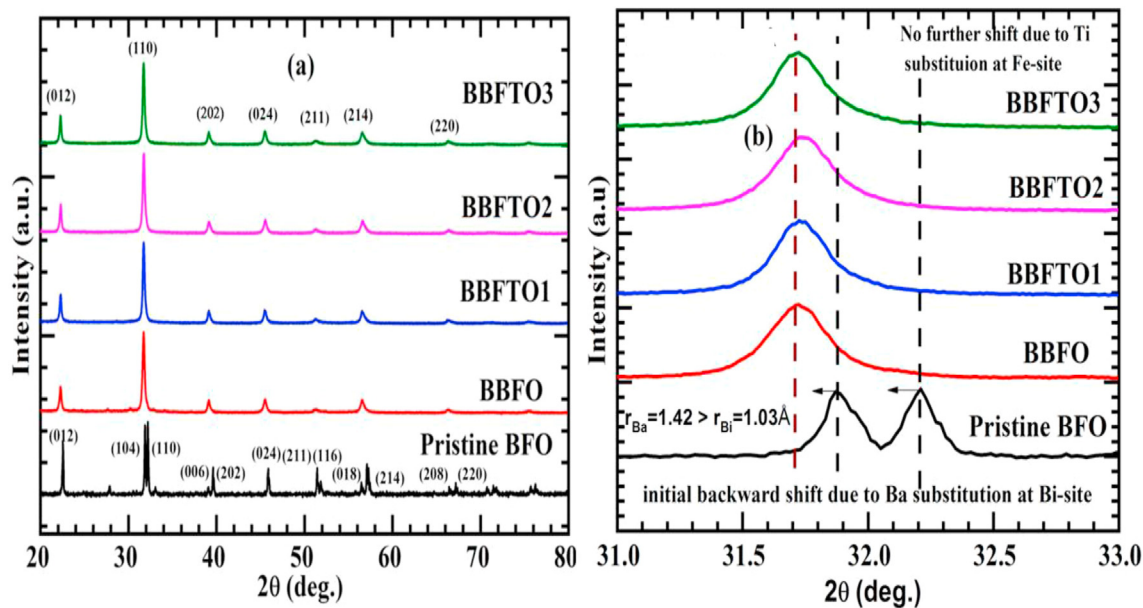
Figure 1. (a) XRD pattern of pristine BFO, BBFO, BBFTO1, BBFTO2, and BBFTO3, and (b) enlarge view from 31° to 33°.
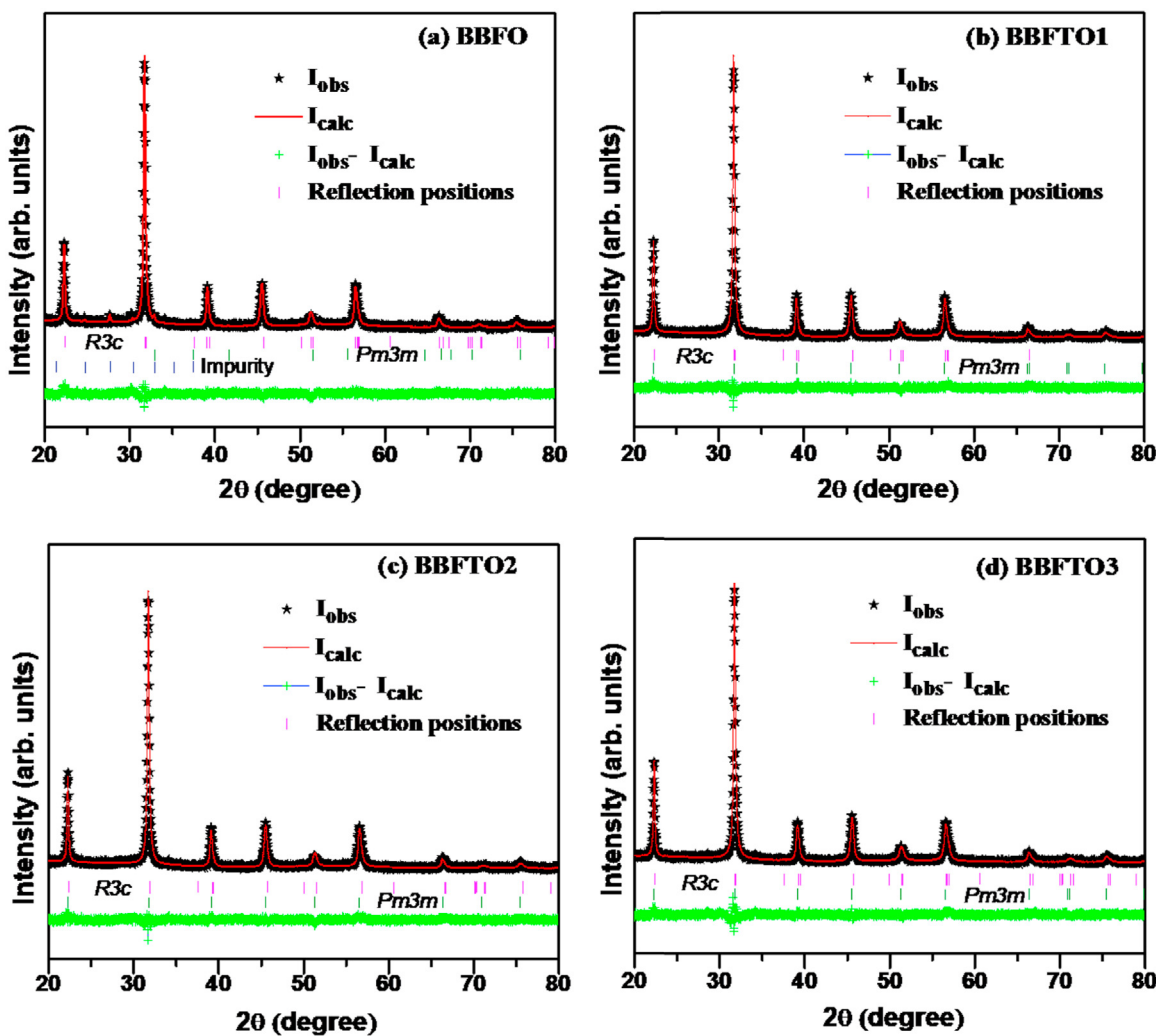
Figure 2. (a), (b), (c), and (d) show the Rietveld refinement for BBFO, BBFTO1, BBFTO2, and BBFTO3 samples.

Table 1. Several structural parameters of BBFO, BBFTO1, BBFTO2 and BBFTO3 samples.

Parameters			BBFO	BBFTO1	BBFTO2	BBFTO3
Wt% Rietveld	Rhombohedral (R3c) phase		24	32	26	31
	Cubic (Pm$\overline{3}$m) phase		76	68	74	69
Lattice parameter	Rhombohedral phase	a (Á)	5.5978	5.6003	5.6095	5.6221
		c (Á)	13.8169	13.7989	13.7301	13.6843
	Cubic phase	a (Á)	3.9849	3.9839	3.9825	3.9821
Volume	Rhombohedral		374.961	374.803	374.165	374.587
	Cubic		63.281	63.232	63.166	63.147
Crystal density (g/cm^3)	R3c		8.313	8.316	8.330	8.321
	Pm$\overline{3}$m		6.172	6.177	6.183	6.185
Rwp			0.0457	0.0530	0.0531	0.0542
Rp			0.0428	0.0418	0.0420	0.0424
GOF			1.675	1.476	1.594	1.644
Fe–O bond length (Á)			1.9416 (4)	1.9417 (3)	1.9448 (2)	1.9420 (7)
Fe–O–Fe bond angle (deg.)			156.178	156.172	156.151	156.134
T			0.897	0.90	0.901	0.899

been reported by Zhang et al. [48] for Pb^{2+} doped BFO and Shahzad et al. for Sr^{2+} doped BFO systems [49].

Thus, Ba^{2+} and Ti^{4+} co-doped samples were fitted to both *R3c* and *Pm$\overline{3}$m* symmetries, resulting in good contract between the calculated and observed patterns. Rietveld refinement shows that both structures co-exist for all samples. Although, complete transformation from rhombohedral to cubic was not observed where *R3c* comprises 24% (76% *Pm$\overline{3}$m*), 32% (68% *Pm$\overline{3}$m*), 26% (74% *Pm$\overline{3}$m*), and 31% (69% *Pm$\overline{3}$m*) of the total amount for BBFO, BBFTO1, BBFTO2 and BBFTO3 samples, respectively. The Goldschmidt tolerance factor (*t*) is used to calculate the degree of distortion in the structure, as defined by the following equation [50]:

$$t = \frac{R_A + R_O}{\sqrt{2}(R_B + R_O)} \quad (1)$$

where R_A, R_O and R_B denotes the ionic radii of A-site cations, oxygen anions and B- site cations, respectively. The above equation for $Bi_{0.80}Ba_{0.20}Fe_{1-x}Ti_xO_3$ compositions can also be used to understand the phase transformation, which can be written as:

$$t = \frac{[(0.80)r_{Bi^{3+}} + (0.20)r_{Ba^{2+}} + r_{O^{2-}}]}{\sqrt{2}[(1-x)r_{Fe^{3+}} + r_{O^{2-}} + xr_{Ti^{4+}}]} \quad (2)$$

where $r_{Bi^{3+}}, r_{Ba^{2+}}, r_{Fe^{3+}}, r_{Ti^{4+}}$ and $r_{O^{2-}}$ represents the Bi^{3+}, Ba^{2+}, Fe^{3+}, Ti^{4+}, and O^{2-}, effective ionic radii, respectively.

The structural phase transition from the perovskite distorted rhombohedral (*R3c*) to pseudocubic (*Pm3m*) or orthorhombic (*Pbnm* or *Pn2$_1$a*) or tetragonal (*P4mm*) primarily depends on type of substitution ions and their concentration, synthesis method, sintering temperature and time as well [51, 52, 53]. At ambient disorders, normally, the structural phase changes occur owing to tilts of octahedra, and the endpoint of phase transition is a cubic (*Pm3m*) symmetry with no tilts [54]. Furthermore, *t* can be used to quantify the structure stability of an ABO$_3$ perovskite compound [37]. For the cubic structure, *t* equals 1. When *t* is less than 1, the octahedral must buckle so as to fit into a too-small cell. We get *t* = 0.897 for BBFO where we used Shannon ionic radii [55] with high spin of Fe^{3+} coordination in 6 folds, and Bi, Fe, Ba, O and Ti in 8 fold coordination. Values for other specimens are given in Table 1. The substitution of Ti^{4+} for Fe^{3+} in BBFTO1 resulted in a slight increase in *t* (to 0.90), implying that the driving force for octahedral rotation will decrease, and leading to a transition from rhombohedral (*R3c*) to cubic (*Pm3m*) structure. However, inclusion of Ti^{4+} at Fe^{3+} site did not change the structure further. Similar result has been reported by Kumar et al. [56] where up to 25%, Ti^{4+} doping did not trigger any structural change.

Figure 3(a) depicts the atomic configurations of the rhombohedral unit cell for the BBFO sample. BFO comprises an oxygen octahedra network, as shown in Figure 3(a), in which two octahedra are joined by sharing their oxygen and distorted FeO$_6$ octahedra are formed with Fe ions surrounded by six neighboring oxygen anions. As discussed before, induction of Ba^{2+} at Bi^{3+} site unbalanced the charge which resulted in generation of oxygen vacancies for charge compensation and there is significant size mismatch between Ba and Bi ions. Both these features will generate strain in the lattice and as a result FeO$_6$ octahedron is distorted resulting in change of bond lengths of Fe–O and bond angle of Fe–O–Fe as displayed in Figure 3(b, c). The variations of bond lengths of Fe–O and bond angles of Fe–O–Fe versus Ti^{4+} concentration is tabulated in Table 2. Furthermore, in *R3c* symmetry, the three short degenerate Fe–O bond lengths, slightly increased as well as three long degenerate Fe–O bond lengths, slightly decreased by due to Ti^{4+} substitution (Figure 3(c)). Variations in Fe–O bond length and Fe–O–Fe bond angle control both super exchange interaction and orbital overlap within O and Fe ions, which is expected to have an impact the systems magnetic and transport properties.

A comparison of average crystallite size for BBFO, BBFTO1, BBFTO2 and BBFTO3 samples was made from XRD analysis. The microstrain due to lattice deformation was estimated using the W–H and SSP methods, and the crystallite sizes obtained using these methods were compared to those obtained using the Scherrer method. The average crystallite size can be calculated using Scherrer's equation and determined from XRD data [57]:

$$D = \frac{k\lambda}{\beta_d cos\theta} \quad (3)$$

where, *D* represents average crystallite size in nanometers, λ denotes the radiation wavelength (0.154056 nm), k indicates a shape factor (= 0.90), β_d denotes the physical broadening of the sample as measured as full width half maximum (FWHM) in radian, θ signifies the position of peak in radian.

A finite crystal size and its corresponding lattice strain are deviations from the perfect crystal, according to Williamson-Hall (W–H). If all of the peaks are shifted in the same direction, It represents the crystal's isotropic nature and vice versa. The broadening of strain-induced peak (β_S) in powders arises from crystal distortion and imperfections which can be calculated by following formula [58]:

$$\varepsilon = \frac{\beta_S}{4tan\theta} \quad (4)$$
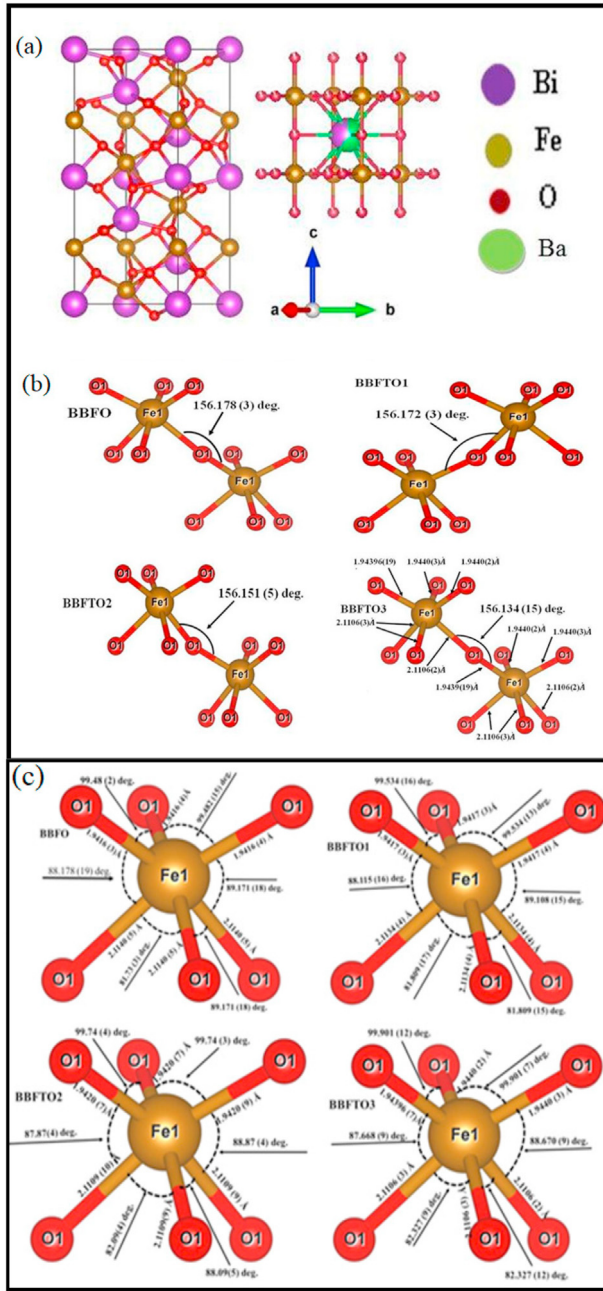
Figure 3. (a) Schematic of crystal structure for BBFO samples, (b) Shows the variation in bond angles of Fe–O–Fe and (c) shows various bond lengths and bond angles (O–Fe–O) for BBFO, BBFTO1, BBFTO2 and BBFTO3 samples.

The Bragg peak breadth is the amalgamation stain broadening as well as effect of particle size from Eqs. (3) and (4), respectively. Thus, the total broadening due to strain and size in a particular peak having hkl value, can be expressed as,

$$\beta_{hkl} = \beta_s + \beta_d \qquad (5)$$

$$\beta_{hkl} = 4\varepsilon tan\theta + \frac{k\lambda}{Dcos\theta} \qquad (6)$$

By rearranging Eq. (6) gives

$$\beta_{hkl}cos\theta = \left(\frac{k\lambda}{D}\right) + (4\varepsilon sin\theta) \qquad (7)$$

Table 2. Bond length Fe–O and bond angle of Fe–O–Fe for BBFO, BBFTO1, BBFTO2 and BBFTO3 samples.

Sample	Fe–O bond length (Å)	O–Fe–O bond angle (°)
BBFO	1.9416 (3)	99.482 (2)
	1.9416 (4)	99.482 (15)
	1.9416 (4)	89.171 (18)
	2.1140 (5)	89.171 (18)
	2.1140 (5)	81.73 (3)
	2.1140 (5)	88.178 (19)
BBFTO1	1.9417 (3)	99.534 (16)
	1.9417 (3)	99.534 (13)
	1.9417 (4)	89.108 (15)
	2.1134 (4)	81.809 (15)
	2.1106 (3)	81.809 (17)
	2.1106 (3)	88.115 (16)
BBFTO2	1.9420 (7)	99.74 (4)
	1.9420 (7)	99.74 (3)
	1.9420 (9)	88.87 (4)
	2.1109 (9)	82.09 (5)
	2.1109 (9)	82.09 (4)
	2.1109 (10)	87.87 (4)
BBFTO3	1.9439 (7)	99.901 (12)
	1.9448 (2)	99.901 (7)
	1.9448 (3)	88.670 (9)
	2.1106 (2)	82.327 (12)
	2.1106 (3)	82.327 (9)
	2.1106 (3)	87.668 (9)

Eq. (7) is known as W–H equation and mentioned as Uniform Deformation Model (UDM) [58], which considers isotropic nature of the crystals. The graph is plotted between $\beta cos\theta$ versus $4sin\theta$ as shown in Figure 4a, b, c, d. These plotted straight line is a well-fitting line that corresponds to all of the values, as the correlation coefficient value of R^2 is 0.955, 0.750, 0.724, 0.747, respectively. The linear fit's slope represents the strain value, and the fitted line's y-intercept represents the crystallite size [58]. In W–H method, the line broadening was isotropic in nature. The size-strain plot is shown in Figure 5a, b, c, d, where the crystal is considered to non-uniform with orientation of lattice plane in all crystallographic directions. The size-strain plot (SSP) method produces a better size-strain profile by describing the crystallite size with a Lorentzian function and the strain profile with a Gaussian function [59, 60]. So, the SSP calculation is performed using the equation [61], as follow

$$(d_{hkl}\beta_{hkl}cos\theta_{hkl})^2 = \frac{K\lambda}{D}\left(d_{hkl}^2\beta_{hkl}cos\theta_{hkl}\right) + \left(\frac{\varepsilon_a}{2}\right)^2 \qquad (8)$$

where d_{hkl} is lattice spacing, K denotes a constant that varies with particle shape (3/4 for spherical particles), and ε_a indicates evident strain. $d_{hkl}^2\beta_{hkl}cos\theta_{hkl}$ is along x-axis and $(d_{hkl}\beta_{hkl}cos\theta_{hkl})^2$ along y-axis. The microstrain is calculated from the root of the y-intercept, and the slope of the linearly fitted data gives the crystallite size.

Table 3 summarizes the results of the Scherrer, W–H, and SSP methods for estimating average crystallite size and microstrain of BBFO, BBFTO1, BBFTO2, and BBFTO3 samples. The entire method demonstrates that a non-zero intercept and the line through points have a positive slope, indicating that they are isotropic [62]. The measurement trend of the crystallite size in all samples is same. Figure 6 shows a comparative study of different methods. We can note that the average microstrain in SSP is higher than the W–H method. The variation in average crystallite size in the D-S method is less than that in the W–H and SSP methods due to the distribution of the difference in average particle size. By looking at the graphs, it has been observed that there is anomalous crystallite size which first increased then decreased and again
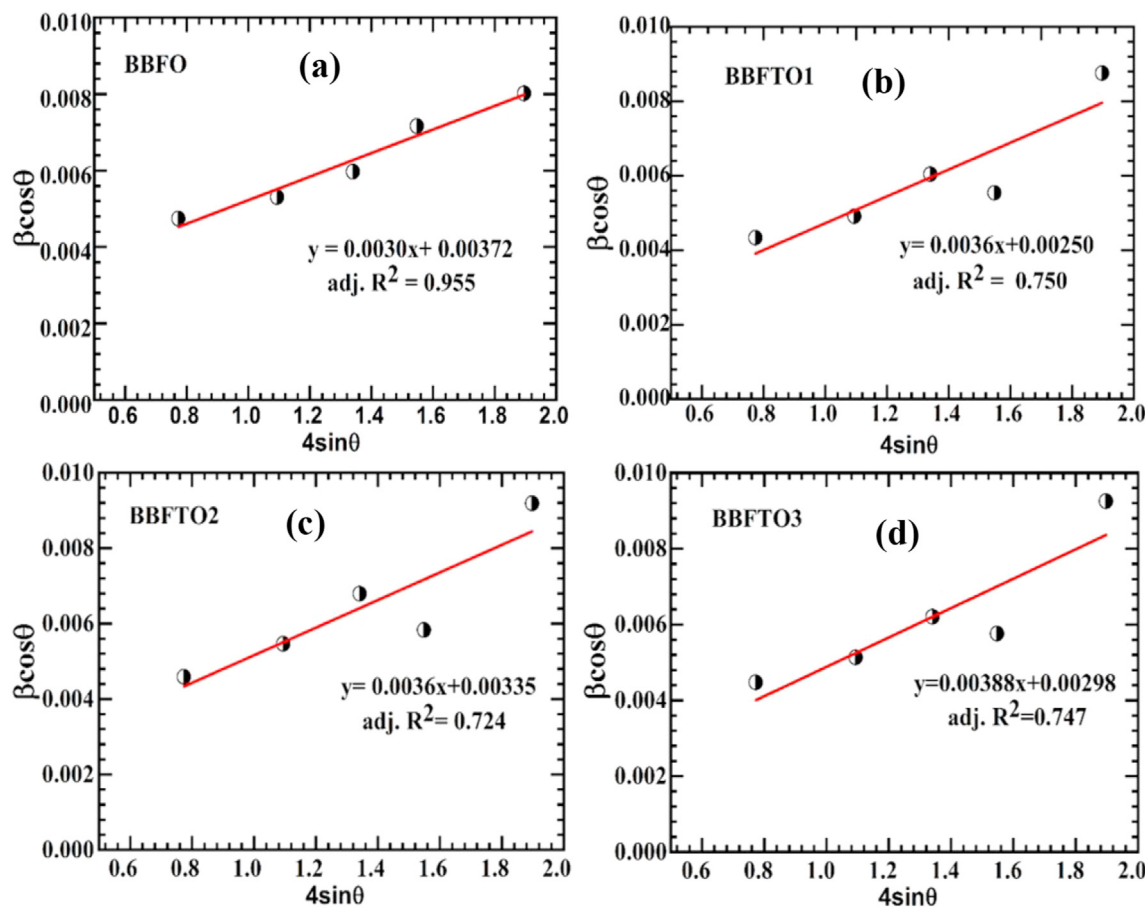
Figure 4. (a), (b), (c) and (d) show the crystallite size for BBFO, BBFTO1, BBFTO2, and BBFTO3 samples using W–H method.

increased significantly. This anomaly indicated that domain is segregated thought the lattice structure. SSP method gives more accurate crystallite size and is in good agreement with the Scherrer method.

3.2. Morphological analysis

Figure 7 shows FESEM images of BBFO, BBFTO1, BBFTO2, and BBFTO3 samples. All samples showed similar morphology and the grains are non-uniform with varying sizes. Histogram regarding the particle size distributions is also shown in Figure 7. Except for x = 0.02, the average particle size decreases as Ti^{4+} concentration increases. Similar findings have earlier been reported in the literature [46]. It has been proposed that grain growth is influenced by the oxygen vacancies concentration [7, 63] as well as the ion diffusion rate [64]. With increase in Ti^{4+} substitution at Fe^{3+} site, the concentration of oxygen vacancies which were previously produced as a charge reimbursement mechanism owing to Ba^{2+} substitution at Bi^{3+} site will decrease. Hence, reduced oxygen vacancy concentration can lead to decrease in grain size [63]. The substitution of Ti^{4+} concentration may have inhibited grain boundary growth. As a result, as Ti^{4+} concentration increases, the average particle size decreases. Moreover, pores at the grain boundary become much smaller as grain size decreases. The porosity in ceramic samples develops from two sources: inter-granular porosity and intra-granular porosity [65]. Thus the total porosity can be written as, P = Pinter + Pintra. However, the major obstacle originates from the inter-granular type porosity and the ρ_B decreases with the addition of Ti^{4+} may be owing to the inter-granular pores. In addition to this, the observed grains are separated by Ti-rich areas that originate due to the tendency of the Ti^{4+} dopant to segregate from the perovskite lattice [66]. This microstructure may be responsible for the changes produced in both the magnetism and dielectric properties of the present investigation.

3.3. Magnetic behavior in response to a magnetic field

Magnetic properties of BBFO, BBFTO1, BBFTO2 and BBFTO3 samples revealed a distinct correlation between the strain and compositional dependent magnetic phase transformation. Figure 8(a) and (b) shows the M-H hysteresis loops for BBFO, BBFTO1, BBFTO2 and BBFTO3 samples up to maximum applied field of 10 kOe recorded at 298 K and 77 K, respectively. The variation of coercivity, remnant magnetization and saturation magnetization at 298 K and at 77 K versus Ti^{4+} concentration is displayed in Figure 8(c) and (d). At 298 K, all of the samples exhibited weak ferromagnetic behavior. At 298 K and 77 K the value of remnant magnetization (M_r) and saturation magnetization (M_s) were found to decreases with increase of Ti^{4+} concentration which is consistent with Deng et al. [67] observation. On the other hand, a Ti^{4+} concentration of 6% exhibited a maximum value of Hc, after which the Hc decreased, indicating that the system's magnetic anisotropy has decreased. This is important to note that the Hc values are high which could have been caused by magnetic anisotropy effects [37]. It is also widely acknowledged that, in addition to dopant concentration, the presence of defects capable of trapping (pinning) the magnetic domain walls affects the Hc of magnetic materials. Additionally, grain size affects the material's Hc. Therefore, when the Ti^{4+} concentration exceeded 6%, the Hc decreased, indicating a change in grain size or these imperfections that reduces magnetic anisotropy and thus Hc. The behavior of Hc in the present study is consistent with previously reported literature [68]. However, surprisingly at low temperature with the increase of Ti^{4+} concentration, the BBFTO3 sample exhibited diamagnetic behavior. Pure BFO is known to have G-type canted antiferromagnetic structure which is superimposed by a spiral spin structure with a 62 nm period length that cancels out net magnetization [69]. Therefore, pure BFO at room temperature is antiferromagnetic (not shown here). The introduction of 20% Ba at Bi-site
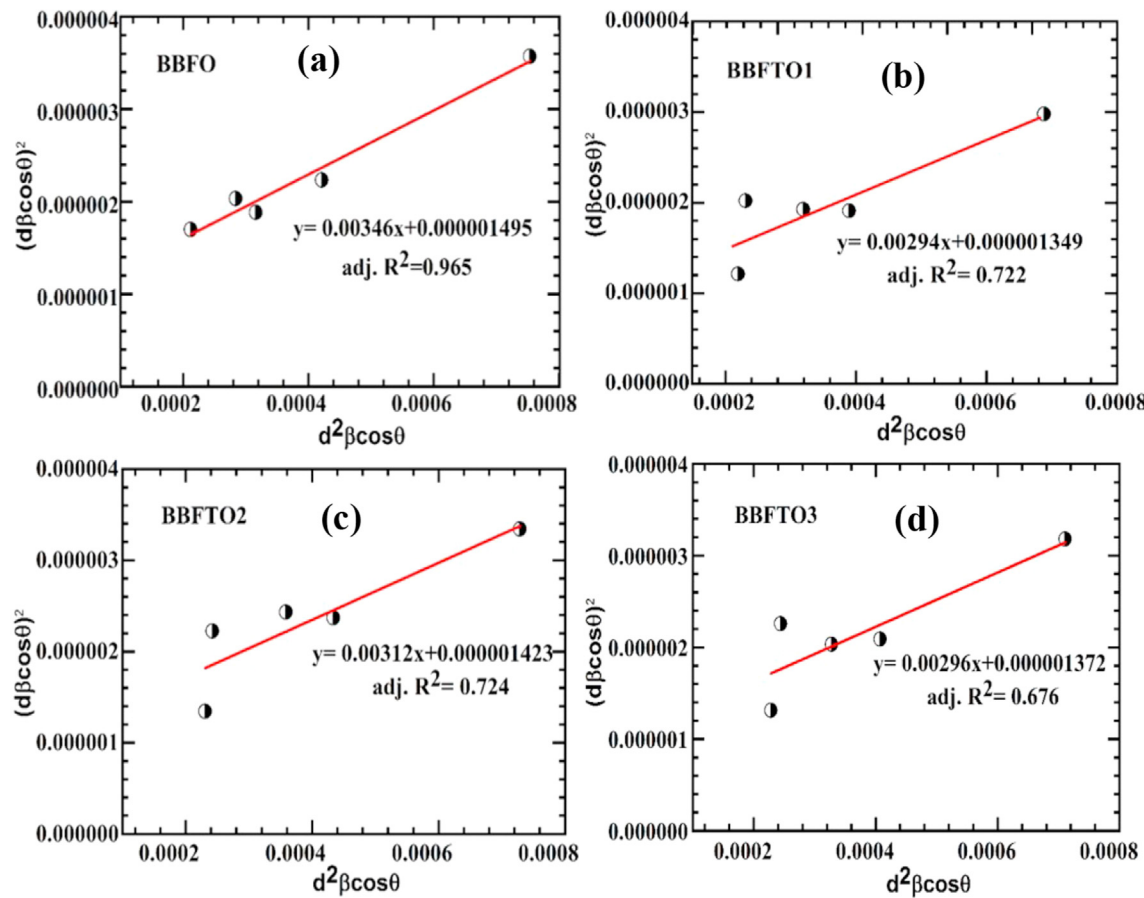
Figure 5. (a), (b), (c), and (d) show the crystallite size for BBFO, BBFTO1, BBFTO2, and BBFTO3 samples using SSP method.

Table 3. Average particle size and microstrain of BBFO, BBFTO1, BBFTO2 and BBFTO3.

Sample	Crystallite Size, D (nm)			Strain, $\varepsilon \times 10^{-3}$	
	$D_{D\text{-}S}$	D_{WH}	D_{SSP}	ε_{W-H}	ε_{SSP}
BBFO	30.66	37.27	33.40	3.00	2.45
BBFTO1	32.87	55.46	39.30	3.60	2.32
BBFTO2	29.87	41.38	37.03	3.60	2.37
BBFTO3	36.52	46.52	39.03	3.88	2.34

(BBFO sample) exhibited ferromagnetic behavior. There are various possible ways to induce magnetization in BFO. The first reason is the suppression of cycloid spin structure due to phase transformed to pseudo cubic which has been confirmed by XRD analysis [49, 70]. This, transformation can frustrate the long range inhomogeneous spiral spin structure and unlock the net magnetization [70]. Moreover, other structural changes produce by lattice strains have a substantial effect on magnetic properties. There are two possible sources of strains, (i) due to large variance in ionic radius of Bi^{3+} (1.17 Å) and Ba^{2+} (1.42 Å), and (ii) presence of oxygen vacancies caused by a charge compensation mechanism [37, 49]. Both these effects can change the bond lengths of Fe–O and the bond angles of Fe–O–Fe which are given in Table 2. Oxygen vacancy may also change the coordination of Fe from octahedral to tetrahedral which can shift bond angle of Fe–O–Fe and affect the strength of superexchange interaction [37]. It has been reported that the super-exchange interaction that results in the antiferromagnetic behavior of the BFO system is extremely sensitive to bond angles and distances [37]. This clearly indicates that changes in the FeO local environment caused by induced lattice strains would affect the super-exchange
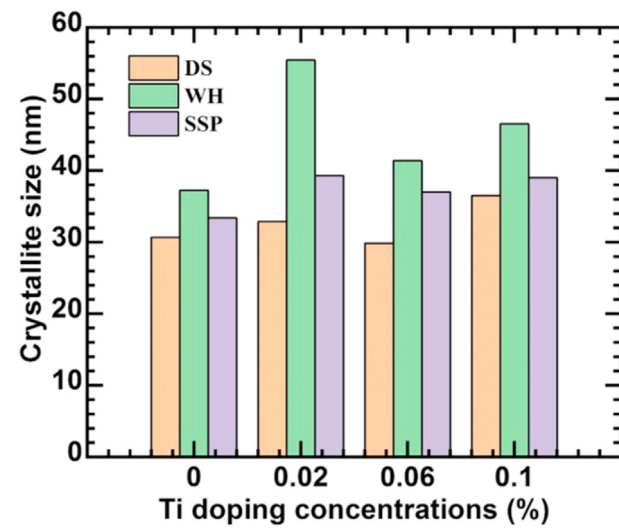
Figure 6. A comparison crystallite size study using three types of methods.

interaction and thus magnetization. Therefore, the induced lattice strains have profound role in generation of magnetization in Ba doped BFO. Moreover, it can be noted that H_c value for BBFO sample decreases at 77 K, this decrease of H_c at low temperature can be a signature of ME coupling in the materials [71]. The introduction of Ti^{4+} at Fe^{3+}-site decreases the M_r, M_s and H_c significantly both at 298 K and 77 K. This is understandable as the Ti^{4+} is non-magnetic so their replacement for magnetic Fe^{3+} will reduce magnetization in the system. The decrease in
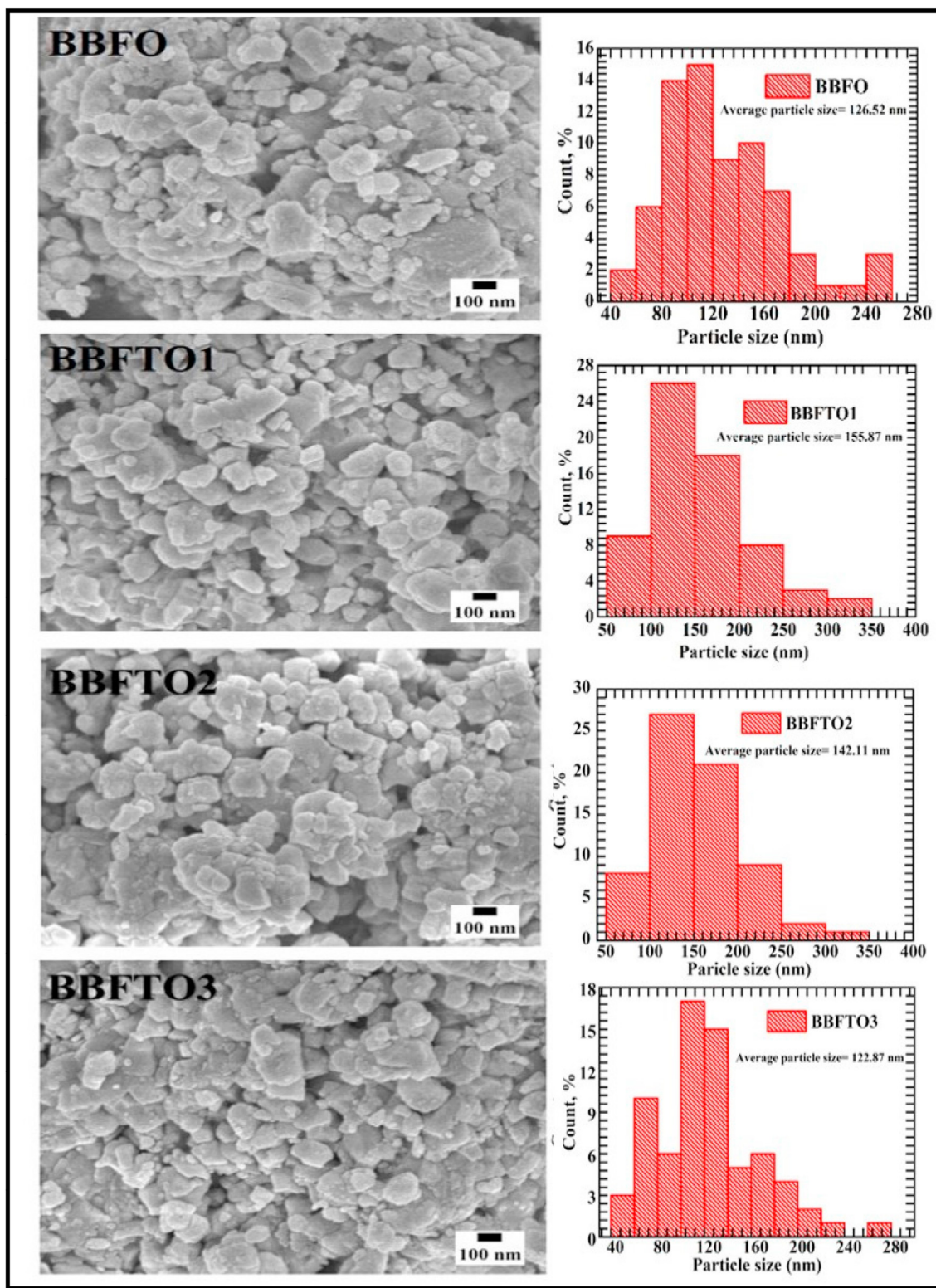
Figure 7. FESEM images of BBFO, BBFTO1, BBFTO2, BBFTO3 and their corresponding histogram.

magnetic coercivity with increase in Ti^{4+} substitution (except for BBFTO3) indicates decrease of magnetic anisotropy of the system.

3.4. Complex permeability

Permeability is one of the main features of ferromagnetic materials in explaining magnetic properties. The complex permeability can be repre-

sented by $\mu^* = \mu' - j\mu''$ [72], where μ' is real part and μ'' is imaginary part. The μ' and μ'' expresses the energy stored up and energy dissipation in the system when the magnetic induction vector (B) component is in phase and out of phase with alternating magnetic field (H), respectively. The μ' increases with increase in frequency up to 1 kHz then show some resonance peaks in the range of 1 kHz–10 kHz as shown in Figure 9(a). These peaks are known as limiting frequency or cut-off frequency [73]. At high
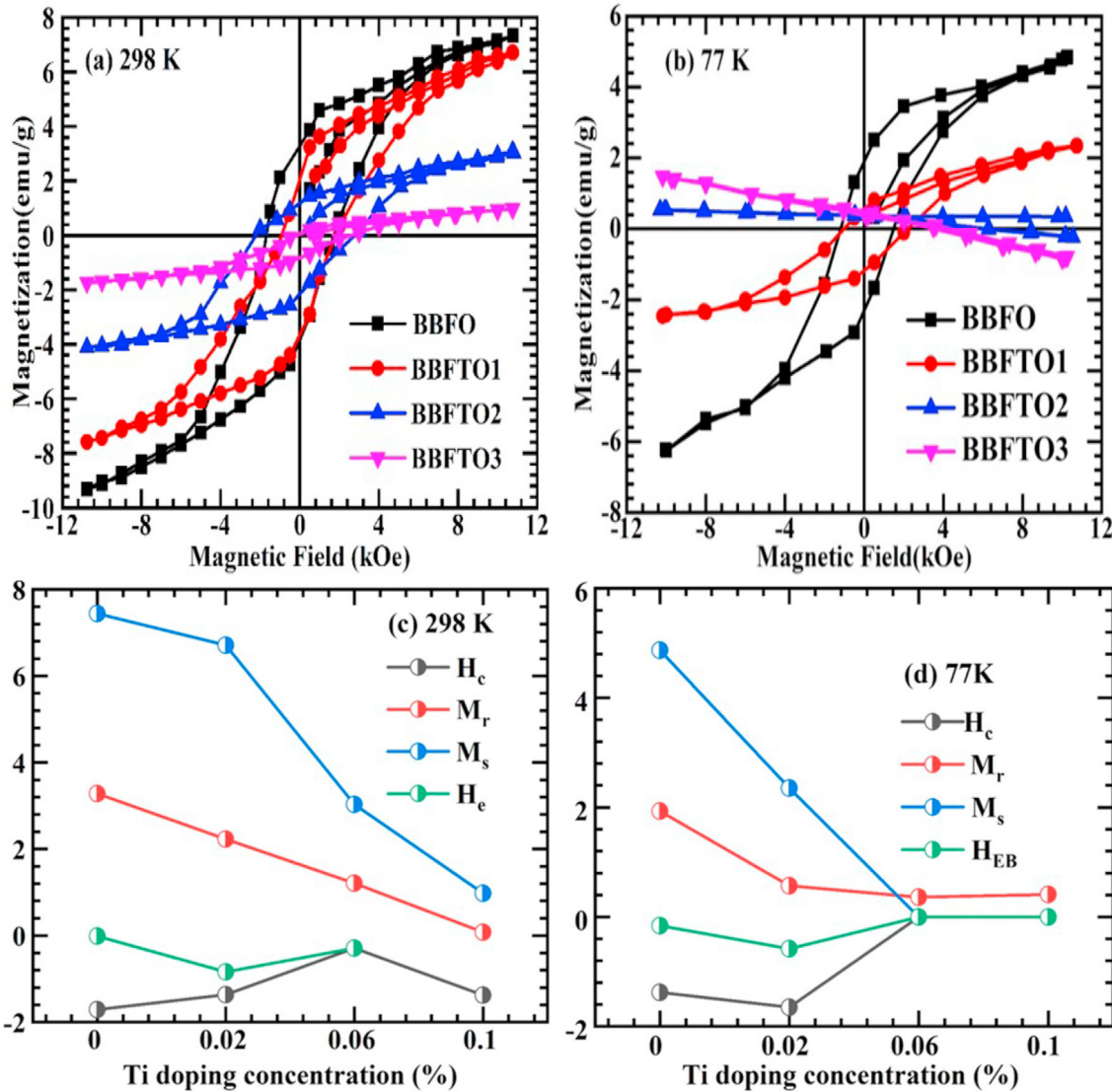
Figure 8. M-H loops of BBFO, BBFTO1, BBFTO2, and BBFTO3 samples at (a) 298 K and (b) 77 K. (c) and (d) shows the variations of coercivity, remnant magnetization, saturation magnetization and exchange bias field as a function of Ti concentration.

frequency, the value of μ' nearly constant which might be due to domain wall relaxation [74, 75]. We can also note that Ti^{4+} doped systems have small values of μ' at all frequencies compared to the BBFO sample which is consistent with the fact that Ti^{4+} is a non-magnetic ion. Imaginary relative permitivity (μ'') shows high values at low frequencies which decrease rapidly with increase in frequency as revealed in Figure 9 (b). The μ'' remains almost frequency independent after 1 kHz. It is well known that the appearance of μ'' is due to the lagging of the motion of the domain walls with the applied alternating magnetic field [74]. In the present work, μ'' exhibits a much higher value at low frequencies. It may be due to irreversible displacement of domain walls [76]. An earlier study made a similar observation [77]. Figure 9(c) depicts the magnetic loss variant with frequency, which shows no noticeable change with Ti^{4+} content. The magnetic loss factor in Figure 9(c) decreases with increasing frequency which may be due to the advancing of domain wall motion as well as uniformity of microstructure [78].

The plot of relative quality factor, RQF, ($RQF = \frac{\mu'}{\mu_m''}$) with frequency is displayed in Figure 9(d). In practical, RQF is a measure of efficiency of a magnetic material. Figure shows that Q-factor increase with increasing frequency (except for BBFTO3 which show diamagnetic trend) without

any peak. We can notice a shift in Q-factor values towards lower frequency side with increase in Ti^{4+} content.

3.5. Dielectric behavior as a function of frequency and temperature

The frequency dependence of dielectric constant (ε) and dielectric loss ($tan\delta$) for BBFO, BBFTO1, BBFTO2, and BBFTO3 samples at RT is shown in Figure 10(a) and (b). At low frequencies, the ε is high and sharply decreases with increase in frequency up to about 1 kHz, thereafter it becomes almost frequency independent for all samples. Furthermore, the $tan\delta$ variation with frequency showed a similar decreasing trend. The value of ε at lower frequencies is attributed to the contribution from different localized charge defects such as space charge, permanent dipoles, induced atomic and ionic dipoles which play a part to contributing high dielectric values [49]. The large dielectric dispersion observed for all samples is ascribed to the Maxwell-Wanger interfacial type polarization [79]. The cause is that while the applied field is followed by the defect dipoles at lower frequencies, as the frequency rises, the dipoles start to lag the field, which causes the value of ε to fall. Materials that are dielectric and ferroelectric frequently exhibit this kind of behavior [80].
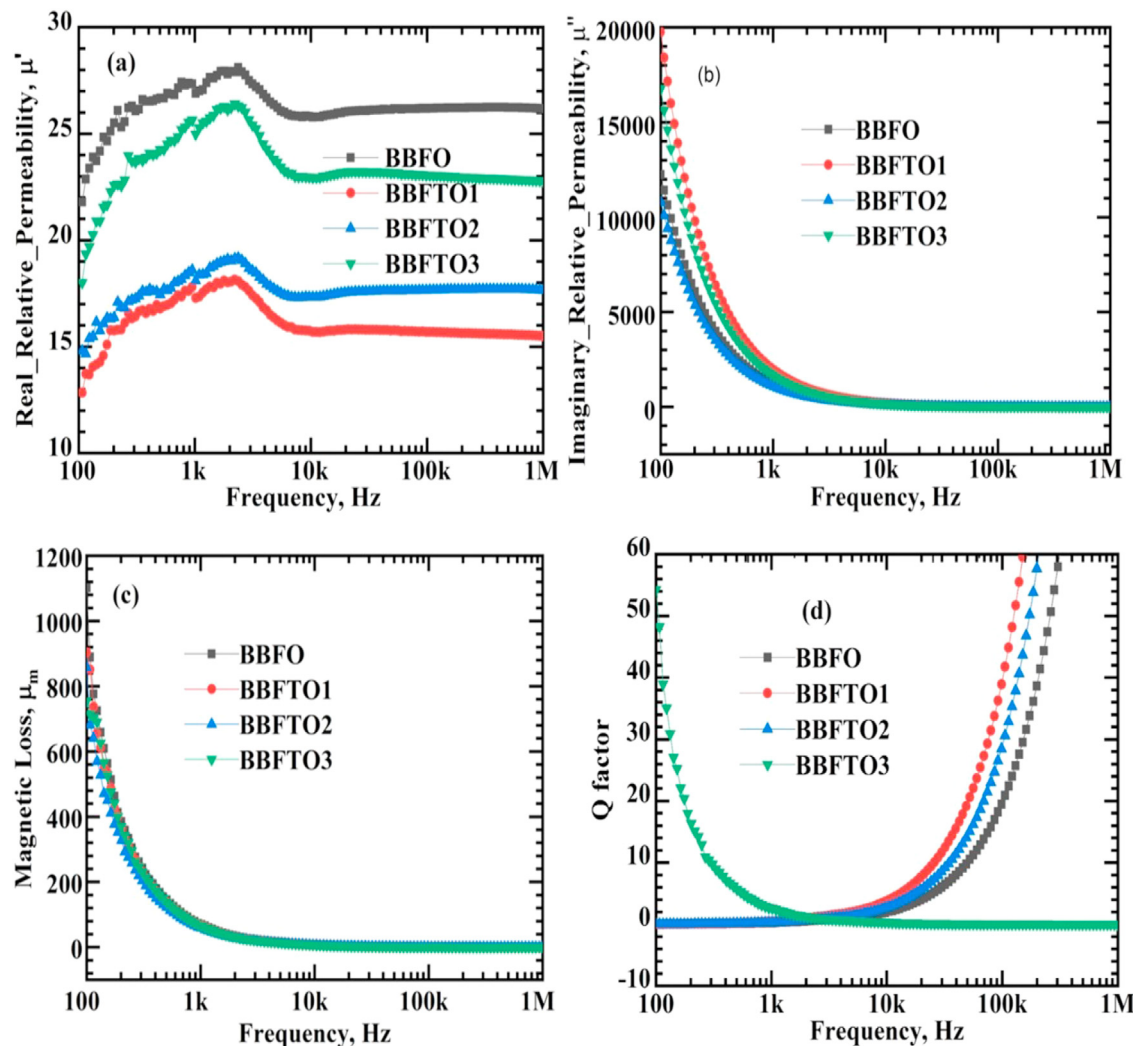
Figure 9. (a), (b), (c) and (d) show the frequency dependence of real permeability, imaginary permeability, magnetic loss and relative quality factor (Q-factor) for BBFO, BBFTO1, BBFTO2, and BBFTO3 samples.

Due to Pb^{2+} or Ba^{2+} substitution, Deng et al. [67] and Mazumder et al. [81] both showed similar outcomes. At lower frequencies, the highest value of ε is found for BBFO sample. This high value of ε in BBFO composition could also be due to structural distortion in the sample. In the present study Ba^{2+} substituted in Bi^{3+} induce defect in the lattice. Thereby increases the oxygen vacancy, resulting in the increase of space charge. Thus, for BBFO at low frequency show a high value of ε. Such behavior is found for BBFO in the earlier literature [82]. Conversely, the lowest value is obtained for BBFTO3 sample This is the expected trend as we know that BBFO (20% Ba^{2+} at Bi^{3+}-site in BFO) sample, has highest content of oxygen vacancies (induced defects) in the lattice and as a result shows high value of ε at lower frequency region [82]. On the other hand, the Ti^{4+} doped BBFTO1, BBFTO2 and BBFTO3 samples showed that dielectric constant decreases consistently at lower frequencies which is ascribed to a significant decrease of oxygen vacancies due to charge compensation. Thus, BBFTO1, BBFTO2 and BBFTO3 have fewer defects which is also evident from the dielectric loss trend. We can note the $tan\delta$ decreases at all frequencies with increase in Ti^{4+} content (Figure 10 (b)) except for BBFTO3. Although no unreacted component is visible in XRD phase identification, this could be due to the presence of impurity in the samples. The results are consistent with those previously reported [46].

Temperature dependence of ε and $tan\delta$ for BBFO, BBFTO1, BBFTO2 and BBFTO3 samples at 10 kHz are shown in Figure 10(c) and (d). Both the ε and $tan\delta$ are found to rise with increase in temperature up to a

maximum given temperature of 670 K. However, a peak in the dielectric constant has been observed for BBFO sample around 550 K. All the other Ti^{4+} doped samples shows regular increasing trend with no peak. The dielectric anomaly observed at 550 K for BBFO sample might be related the antiferromagnetic to paramagnetic transition. We know that undoped BFO shows antiferromagnetic to paramagnetic transition around 640 K. 20% Ba incorporation at Bi^{3+} side (BBFO sample) might shift this transition to lower temperature [83]. Das et al. [29] reported similar decrease in transition temperature for Ba^{2+} incorporation in BFO in their studied temperature and field dependent magnetic data. Moreover, Ti^{4+} doped samples do not show such transition in the studied temperature range indicating that the transition temperature has been shifted to higher temperatures and lie outside the studied temperature window.

The $tan\delta$ begins with a small value at RT, as shown in Figure 10(b). It starts to rise slowly as temperature rises, reaching a peak around 550 K for BBFTO3 sample. Other ferrites showed similar behavior [84]. It was noted that a change in the conduction mechanism is what is responsible for the maximum in $tan\delta$. Furthermore, if the dielectric material is a mixture of two or more polar substances, the dependence of $tan\delta$ (T) may have two or more maxima produced by the effect of the mixture's separate components [85].

According to Koops' proposed phenomenological model, which assumes that the material is made up of grains and grain boundaries with various parameter values, one can anticipate that each of the grains and grain boundaries will have a unique peak in $tan\delta$ [86]. Therefore, the
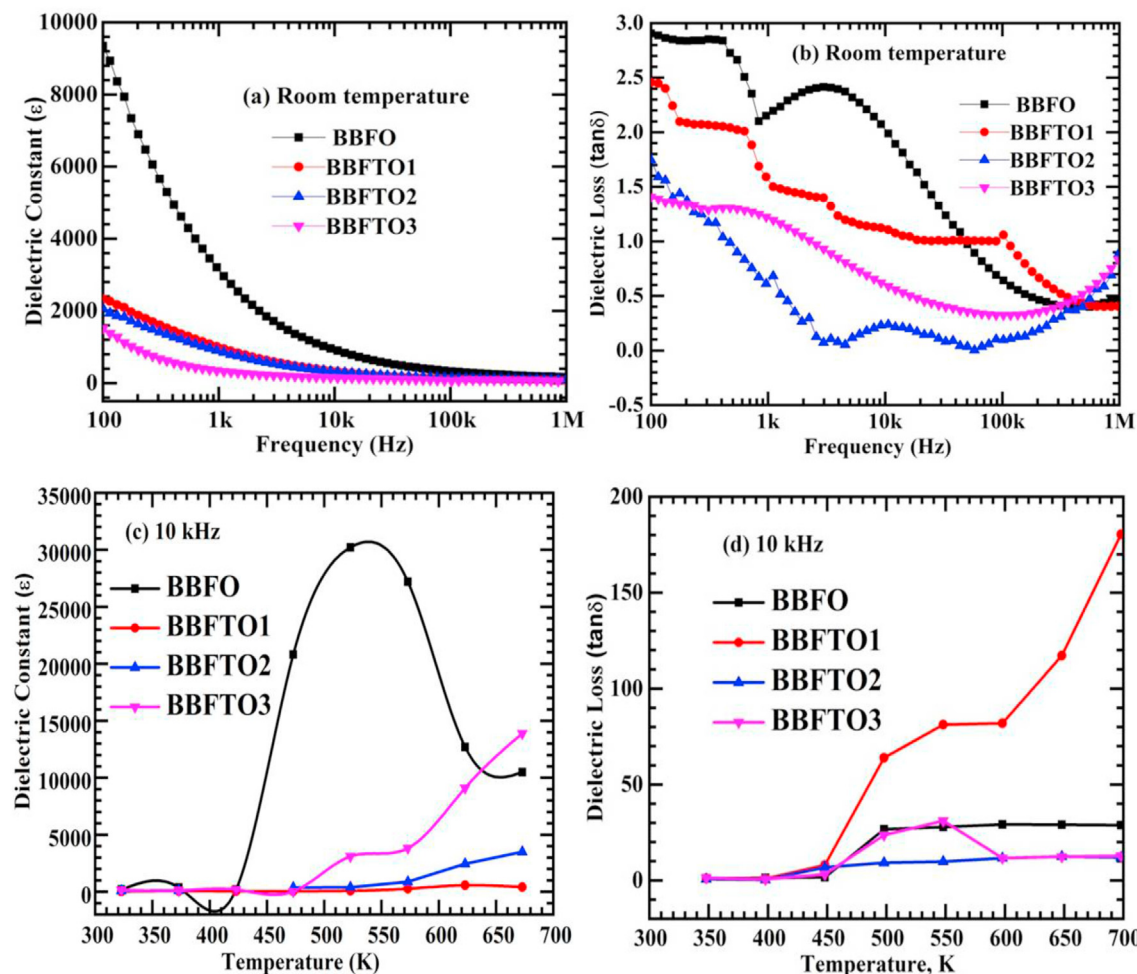
Figure 10. Frequency dependence of (a) dielectric constant and (b) dielectric loss for BBFO, BBFTO1, BBFTO2, and BBFTO3 samples at room temperature. (c) and (d) Temperature dependence dielectric constant and dielectric loss of BBFO, BBFTO1, BBFTO2 and BBFTO3 samples at 10 kHz.

peak in *tanδ* at 550 K may be ascribed to the dielectric loss caused by polarization in the grain boundaries, as opposed to the other peak, which is caused by polarization within the grains.

4. Conclusion

In this study, Ba and Ti co-doped multiferroic ceramics $Bi_{0.80}Ba_{0.20}Fe_{1-x}Ti_xO_3$ ($0 \le x \le 0.10$) have been synthesized by planetary ball milling as well as solid state reaction technique and their local structural, microstructural, magnetic and dielectric properties have been investigated thoroughly. Rietveld analysis of XRD data confirmed that for 20% Ba doped BFO (BBFO) sample, structure has transformed from *R3c* (rhombohedral) to *Pm3̄m* (pseudo-cubic) symmetry. However, no further phase transformation has been observed for Ti doped sample. The average crystallite size and strain shows a band range from 20 nm to 50 nm and $(2 - 3) \times 10^{-3}$, respectively. At room temperature, all the samples are ferromagnetic in nature, however, decrease in magnetization has been observed for Ti doped samples. Presence of magnetization has been explained based on (i) destruction of spiral spin structure and (ii) change in Fe—O—Fe canting angle produced owing to size mismatch (between substituent and dopant) and formation of oxygen vacancies. On the other hand, decrease of magnetic moment for Ti^{4+} doped samples can be understood as Ti^{4+} ions are non-magnetic in nature and reduce oxygen vacancies. Interestingly, at low temperatures, a magnetic phase transition from ferromagnetic to diamagnetic has been observed. At room temperature, 20% Ba doped BBFO shows higher value of dielectric constant at low frequencies due high density of defect (oxygen vacancy and crystal

defect). The introduction of Ti significantly reduced the concentration of defects and improved dielectric properties.

Data availability statement

Data will be made available on request.

Declaration of interests statement

The authors declare no competing interests.

Additional information

No additional information is available for this paper.

Acknowledgements

References

[1] M.A. Green, A. Ho-Baillie, H.J. Snaith, The emergence of perovskite solar cells, Nat. Photonics 8 (2014) 506–5014.

[2] R. Ramesh, N.A. Spaldin, Multiferroics: progress and prospects in thin films, Nat. Mater. 6 (2007) 21–29.

[3] W. Eerenstein, N. Mathur, J.F. Scott, Multiferroic and magnetoelectric materials, Nature 442 (2006) 759–765.

[4] C. Ederer, N.A. Spaldin, Weak ferromagnetism and magnetoelectric coupling in bismuth ferrite, Phys. Rev. B 71 (2005), 060401.

[5] B.C. Das, A.K.M. Akther Hossain, Rietveld refined structure, ferroelectric, magnetic and magnetoelectric response of Gd-substituted Ni–Cu–Zn ferrite and Ca, Zr co-doped BaTiO$_3$ multiferroic composites, J. Alloys Compd. 867 (2021), 159068.

[6] M.K. Das, B.C. Das, S.C. Mazumdar, M.N.I. Khan, Hidekazu Tanaka, A.K.M. Akther Hossain, Rietveld refined crystal structure, magnetic, dielectric, and electric properties of Li- substituted Ni-Cu-Zn ferrite and Sm, Dy co-doped BaTiO$_3$ multiferroic composites, Ceram. Int. (2022), 34949.

[7] N.A. Hill, Why are there so few magnetic ferroelectrics?, "Why are there so few magnetic ferroelectrics? J. Phys. Chem. B 104 (2000) 6694–6709.

[8] M. Shariq, S. Hussain, M. Rafique, M. Naveed-Ul-Haq, A. Rehman, Enhanced multiferroic response in new binary solid solution (0.5)Bi$_{0.70}$A$_{0.30}$FeO$_3$–(0.5) PbTi$_{0.5}$Fe$_{0.5}$O$_3$ (A = Sr, Pb, and Ba) systems, J. Magn. Magn Mater. 492 (2019), 165685.

[9] G. Catalan, J.F. Scott, Physics and applications of bismuth ferrite, Adv. Mater. 21 (2009) 2463–2485.

[10] S. Hussain, S. Hasanain, G.H. Jaffari, S.I. Shah, Thickness dependent magnetic and ferroelectric properties of LaNiO$_3$ buffered BiFeO$_3$ thin films, Curr. Appl. Phys. 15 (2015) 194–200.

[11] Yong Li, Xiaoyong Fang, Maosheng Cao, Thermal frequency shift and tunable microwave absorption in BiFeO$_3$ family, Sci. Rep. 6 (2016), 24837.

[12] M.M. Rhaman, M.A. Matin, M.A. Al Mamun, A. Hussain, M.N. Hossain, B.C. Das, M.A. Hakim, M.F. Islam, Enhanced electrical conductivity and multiferroic property of cobalt-doped bismuth ferrite nanoparticles, J. Mater. Sci. Mater. Electron. 31 (2020) 8727–8736.

[13] G. Catalan, J.F. Scott, Physics and applications of bismuth ferrite, Adv. Mater. 21 (2009) 2463–2485.

[14] J. Seidel, L.W. Martin, Q. He, Q. Zhan, Y.-H. Chu, A. Rother, M.E. Hawkridge, P. Maksymovych, P. Yu, M. Gajek, N. Balke, S.V. Kalinin, S. Gemming, F. Wang, G. Catalan, J.F. Scott, N.A. Spaldin, J. Orenstein, R. Ramesh, Conduction at domain walls in oxide multiferroics, Nat. Mater. 8 (2009) 229–234.

[15] C.-H. Yang, J. Seidel, S.Y. Kim, P.B. Rossen, P. Yu, M. Gajek, Y.H. Chu, L.W. Martin, M.B. Holcomb, Q. He, P. Maksymovych, N. Balke, S.V. Kalinin, A.P. Baddorf, S.R. Basu, M.L. Scullin, R. Ramesh, Electric modulation of conduction in multiferroic Ca-doped BiFeO$_3$ films, Nat. Mater. 8 (2009) 485–493.

[16] C.P. Bhole, Antiferromagnetic to paramagnetic phase transitions in bismuth ferrite(BiFeO$_3$) ceramics by solid state reaction, Ceram.-Silikáty 56 (2012) 127–129.

[17] S.-W. Cheong, M. Mostovoy, Multiferroics: a magnetic twist for ferroelectricity, Nat. Mater. 6 (2007) 13–20.

[18] T. Moriya, Anisotropic superexchange interaction and weak ferromagnetism, Phys. Rev. 120 (1960) 91–98.

[19] Min Zhang, Hui-Jing Yang, Yong Li, Wen-Qiang Cao, Xiao-Yong Fang, Jie Yuan, Mao-Sheng Cao, Cobalt doping of bismuth ferrite for matched dielectric and magnetic loss, Appl. Phys. Lett. 115 (2019), 212902.

[20] H.A. Reshi, A.P. Singh, S. Pillai, T.A. Para, S.K. Dhawan, V. Shelke, X-band frequency response and electromagnetic interference shielding in multiferroic BiFeO$_3$ nanomaterials, Appl. Phys. Lett. 109 (2016), 142904.

[21] J.G. Wu, Z. Fan, D.Q. Xiao, J.G. Zhu, J. Wang, Multiferroic bismuth ferrite-based materials for multifunctional applications: ceramic bulks, thin films and nanostructures, Prog. Mater. Sci. 84 (2016) 335–402.

[22] F. Wen, N. Wang, F. Zhang, Enhanced microwave absorption properties in BiFeO3 ceramics prepared by high-pressure synthesis, Solid State Commun. 150 (2010) 1888–1891.

[23] R. Agarwal, Y. Sharma, S. Hong, R.S. Katiyar, Modulation of oxygen vacancies assisted ferroelectric and photovoltaic properties of (Nd, V) co-doped BiFeO$_3$ thin films, J. Phys. D Appl. Phys. 51 (2018), 275303.

[24] Y. Sharma, R. Agarwal, L. Collins, Q. Zheng, A.V. Ievlev, R.P. Her mann, V.R. Cooper, S. Kc, I.N. Ivanov, R.S. Katiyar, S.V. Kalinin, H.N. Lee, S. Hong, T.Z. Ward, Self-assem bled room temperature multiferroic BiFeO$_3$ -LiFe$_5$O$_8$ nanocomp osites, A dv. Funct. Mater. 30 (2019), 1906849.

[25] T. Wang, S.H. Song, Q. Ma, M.L. Tan, J.J. Chen, Highly improved multiferroic properties of Sm and Nb co-doped BiFeO$_3$ ceramics prepared by spark plasma sintering combined with sol-gel powders, J. Alloys Compd 795 (2019) 60–68.

[26] Y. Sharma, R. Agarwal, C. Phatak, B. Kim, S. Jeon, R.S. Katiya r, S. Hong, Long-range stripe nanodomains in epitaxial (110) BiFeO$_3$ thin films on (100) NdGaO$_3$ substrate, Sci. Rep. 7 (2017) 4857.

[27] R. Agarwal, Y. Sharma, R.S. Katiyar, Switchable photovoltaic and polarization modulated rectification in Si-integrated Pt/(Bi$_{0.9}$Sm$_{0.1}$)(Fe$_{0.97}$Hf$_{0.03}$)O$_3$/LaNiO$_3$ heterostructures, Appl. Phys. Lett. 107 (2015), 162904.

[28] D. Wang, W. Goh, M. Ning, C. Ong, Effect of Ba doping on magnetic, ferroelectric, and magnetoelectric properties in mutiferroic BiFeO$_3$ at room temperature, Appl. Phys. Lett. 88 (2006), 212907.

[29] R. Das, K. Mandal, Magnetic, ferroelectric and magnetoelectric properties of Ba-doped BiFeO$_3$, J. Magn. Magn Mater. 324 (2012) 1913–1918.

[30] G. Dhir, P. Uniyal, N. Verma, Multiferroic properties of Sr-doped BiFeO$_3$ nanoparticles, Phys. B Condens. Matter 531 (2018) 51–57.

[31] V. Khomchenko, D. Kiselev, J. Vieira, L. Jian, A. Kholkin, A. Lopes, Y. Pogorelov, J. Araujo, M. Maglione, Effect of diamagnetic Ca, Sr, Pb, and Ba substitution on the crystal structure and multiferroic properties of the BiFeO$_3$ perovskite, J. Appl. Phys. 103 (2008), 024105.

[32] L. Peng-Ting, L. Xiang, Z. Li, Y. Jin-Hua, C. Xing-Wang, W. Zhi-Hong, W. Yu-Chuan, W. Guang-Heng, La-doped BiFeO$_3$: synthesis and multiferroic property study, Chin. Phys. B 23 (2014), 047701.

[33] S. Pattanayak, R. Choudhary, S. Shannigrahi, P.R. Das, R. Padhee, Ferroelectric and ferromagnetic properties of Gd-modified BiFeO$_3$, J. Magn. Magn Mater. 341 (2013) 158–164.

[34] Y. Cui, Y. Zhao, L. Luo, J. Yang, H. Chang, M. Zhu, D. Xie, T. Ren, Dielectric, magnetic, and magnetoelectric properties of La and Ti codoped BiFeO$_3$, Appl. Phys. Lett. 97 (2010), 222904.

[35] D.K. Pradhan, R. Choudhary, C. Rinaldi, R. Katiyar, Effect of Mn substitution on electrical and magnetic properties of Bi$_{0.9}$La$_{0.1}$FeO$_3$, J. Appl. Phys. 106 (2009), 024102.

[36] R. Singh, G. Dwivedi, P. Shahi, D. Kumar, O. Prakash, A. Ghosh, S. Chatterjee, Effect of Pr-and Nd-doping on structural, dielectric, and magnetic properties of multiferroic Bi$_{0.8}$La$_{0.2}$Fe$_{0.9}$Mn$_{0.1}$O$_3$, J. Appl. Phys. 115 (2014), 134102.

[37] S. Hussain, F. Khan, N.Z. Ali, S. Hasanain, M. Siddique, M. Rafique, T. Abbas, Strain driven structural phase transformation and correlation between structural, electronic, and magnetic properties of Bi$_{1−x}$Ba$_x$FeO$_3$ (0≤ x≤ 0.30) system, J. Alloys Compd. 701 (2017) 301–309.

[38] Y. Tian, F. Xue, Q. Fu, L. Zhou, C. Wang, H. Gou, M. Zhang, Structural and physical properties of Ti-doped BiFeO$_3$ nanoceramics, Ceram. Int. 44 (2018) 4287–4291.

[39] M.A. Basith, A. Billah, M.A. Jalil, N. Yesmin, M.A. Sakib, E.K. Ashik, S.M.E. Hoque Yousuf, S.S. Chowdhury, M.S. Hossain, S.H. Firoz, B. Ahmmad, The 10% Gd and Ti co-doped BiFeO$_3$: a promising multiferroic material, J. Alloys Compd. 694 (2017) 792–799.

[40] Yong Li, Wen-qiang Cao, Jie Yuan, Da-wei Wang, Mao-sheng Cao, Nd doping of bismuth ferrite to tune electromagnetic properties and increase microwave absorption by magnetic–dielectric synergy, J. Mater. Chem. C 3 (2015) 9276–9282.

[41] B. Yu, M. Li, J. Wang, Z. Hu, X. Liu, Y. Zhu, X. Zhao, Dependence of magnetic properties on the Fe^{2+} ion in Ba-doped BiFeO$_3$ multiferroic films, Thin Solid Films 520 (2012) 4089–4091.

[42] T.A. Anjum, M. Naveed-Ul-Haq, S. Hussain, M. Rafique, Analyses of structure, electronic and multiferroic properties of Bi$_{1−x}$Nd$_x$FeO$_3$ (x= 0, 0.05, 0.10, 0.15, 0.20, 0.25) system, J. Alloys Compd. 820 (2020), 153095.

[43] R. Mahbub, M.F. Islam, Sintering behavior and microstructure development of Ba doped BiFeO$_3$, Int. J. Innovative Technol. Explor. Eng. 3 (2014) 2278.

[44] J. Rout, R. Choudhary, Structural transformation and multiferroic properties of Ba–Mn co-doped BiFeO$_3$, Phys. Lett. 380 (2016) 288–292.

[45] X. Zheng, P. Chen, N. Ma, Z. Ma, D. Tang, Synthesis and dielectric properties of BiFeO$_3$ derived from molten salt method, J. Mater. Sci. Mater. Electron. 23 (2012) 990–994.

[46] S.C. Mazumdar, F. Alam, U.H. Tanni, K. Kali, B.C. Das, M.N.I. Khan, Effect of Ti^{4+} doping on structural, electrical and magnetic properties of Ni$_{0.4}$Cu$_{0.2}$Zn$_{0.4}$Fe$_{2-x}$Ti$_x$O$_4$ ferrites, Mater. Sci. Appl. 10 (2019) 733–745.

[47] A. Makhdoom, M. Akhtar, M. Rafiq, M. Hassan, Investigation of transport behavior in Ba doped BiFeO$_3$, Ceram. Int. 38 (2012) 3829–3834.

[48] X. Zhang, Y. Sui, X. Wang, J. Tang, W. Su, Influence of diamagnetic Pb doping on the crystal structure and multiferroic properties of the BiFeO$_3$ perovskite, J. Appl. Phys. 105 (2009), 07D918.

[49] S. Hussain, S. Hasanain, G.H. Jaffari, N.Z. Ali, M. Siddique, S.I. Shah, Correlation between structure, oxygen content and the multiferroic properties of Sr doped BiFeO$_3$, J. Alloys Compd. 622 (2015) 8–16.

[50] V.M. Goldschmidt, Naturwissenschaften 14, 1926, pp. 477–485.

[51] P. Kumar, N. Shankhwar, A. Srinivasan, M. Kar, Oxygen octahedra distortion induced structural and magnetic phase transitions in Bi$_{1−x}$Ca$_x$Fe$_{1−x}$Mn$_x$O$_3$ ceramics, J. Appl. Phys. 117 (2015), 194103.

[52] H. Deng, M. Zhang, Q. Zhong, J. Wei, H. Yan, Efect of Mn dop-ing on multiferroic properties in Bi$_{0.8}$Ba$_{0.2}$FeO$_3$ ceramics, Ceram. Int. 40 (2014) 5869–5872.

[53] P.C. Sati, M. Arora, S. Chauhan, M. Kumar, S. Chhoker, Struc-tural, magnetic, vibrational and impedance properties of Pr and Ti codoped BiFeO$_3$ multiferroic ceramics, Ceram. Int. 40 (2014) 7805–7816.

[54] A. Jindal, A. Agarwal, P. Aghamkar, Structural changes and magnetism in Bi$_{1-x}$Ba$_x$FeO$_3$ (x = 0, 0.1, 0.2, 0.3) nanopowders, Appl. Phys. A 124 (2018) 4.

[55] R.D. Shannon, Revised effective ionic radii and systematic studies of interatomic distances in halides and chalcogenides, Acta Crystallogr. A 32 (1976) 751–767.

[56] M. Kumar, K. Yadav, Study of room temperature magnetoelectric coupling in Ti substituted bismuth ferrite system, J. Appl. Phys. 100 (2006), 074111.

[57] P. Scherrer, Göttinger Nachrichten, Math. Phys. 2 (1918) 98–100.

[58] G.K. Williamson, W.H. Hall, Acta Metall. 1, 1953, pp. 22–31.

[59] M.A. Tagliente, M. Massaro, Nucl. Instrum. Methods Phys. Res. B 266, 2008, pp. 1055–1061.

[60] D. Balzar, H. Ledbetter, Voigt-function modeling in fourier analysis of size- and strain-broadened X-ray diffraction peaks, J. Appl. Crystallogr. 26 (1) (1993) 97–103.

[61] V.D. Mote, Y. Purushotham, B.N. Dole, Williamson-Hall analysis in estimation of lattice strain in nanometer-sized ZnO particles, J. Theor. Appl. Phys. 6 (2012) 6–14.

[62] W.H. Hall, X-ray line broadening in metals, Proc. Phys. Soc. 62 (11) (1949) 741–743.

[63] M.A. Islam, M. Zahidur Rahaman, Md. Mehedi Hasan, A.K.M. Akther Hossain, Analysis of grain growth, structural and magnetic properties of Li-Ni-Zn ferrite under the influence of sintering temperature, Heliyon 5 (2019), e01199.

[64] S. Hussain, S. Khurshid Hasanain, G. Hassnain Jaffari, S. Faridi, F. Rehman, T. Ali Abbas, S. Ismat Shah, Size and lone pair effects on the multiferroic properties of Bi$_{0.75}$A$_{0.25}$FeO$_{3-\delta}$ (A = Sr, Pb, and Ba) ceramics, J. Am. Ceram. Soc. 96 (2013) 3141–3148.

[65] B.C. Das, H. Das, M.A. Matin, A.K.M.A. Hossain, Rietveld refinement analysis and influence of individual phases on the magnetoelectrically coupled (1-x)BSZT+ xNCZGF multiferroic composites, J. Alloys Compd. 881 (2021) 160632.

[66] M.S. Bernardo, T. Jardiel, M. Peiteado, F.J. Mompean, M. Garcia-Hernandez, M.A. Garcia, M. Villegas, A.C. Caballero, Intrinsic compositional inhomogeneities in bulk Ti-doped BiFeO$_3$: microstructure development and multiferroic properties, Chem. Mater. 25 (2013) 1533–1541.

[67] H. Deng, M. Zhang, Z. Hu, Q. Xie, Q. Zhong, J. Wei, H. Yan, Enhanced dielectric and ferroelectric properties of Ba and Ti co-doped BiFeO$_3$ multiferroic ceramics, J. Alloys Compd. 582 (2014) 273–276.

[68] M.M. Rhaman, M.A. Matin, M.N. Hossain, M.N.I. Khan, M.A. Hakim, M.F. Islam, Ferromagnetic, electric, and ferroelectric properties of samarium and cobalt co-doped bismuth ferrite nanoparticles, J. Phys. Chem. Solid. 147 (2020), 109607.

[69] I. Sosnowska, T.P. Neumaier, E. Steichele, Spiral magnetic ordering in bismuth ferrite, J. Phys. C Solid State Phys. 15 (1982) 4835–4846.

[70] S.-T. Zhang, Y. Zhang, M.-H. Lu, C.-L. Du, Y.-F. Chen, Z.-G. Liu, Y.-Y. Zhu, N.-B. Ming, X. Pan, Substitution-induced phase transition and enhanced multiferroic properties of Bi$_{1-x}$La$_x$FeO$_3$ ceramics, Appl. Phys. Lett. 88 (2006), 162901.

[71] S. Hussain, S. Hasanain, G.H. Jaffari, N.Z. Ali, M. Siddique, S.I. Shah, Anomalous temperature dependence of magnetic coercivity and structure property correlations in Bi$_{0.75}$A$_{0.25}$FeO$_3$ (A= Sr, Pb, and Ba) system, J. Mater. Chem. C 5 (2017) 9451–9464.

[72] F. Alam, M.L. Rahman, B.C. Das, A.K.M. Akther Hossain, Effect of Cu^{2+} on structural, elastic and magnetic properties of nanostructured Mn–Zn ferrite prepared by a sol-gel auto-combustion method, Physica B 594 (2020), 412329.

[73] N.-N. Song, H.-T. Yang, H.-L. Liu, X. Ren, H.-F. Ding, X.-Q. Zhang, Z.-H. Cheng, Exceeding natural resonance frequency limit of monodisperse Fe$_3$O$_4$ nanoparticles via superparamagnetic relaxation, Sci. Rep. 3 (2013).

[74] A.K.M. Akther Hossain, M.L. Rahman, Enhancement of microstructure and initial permeability due to Cu substitution in Ni$_{0.50-x}$Cu$_x$Zn$_{0.50}$Fe$_2$O$_4$ ferrites, J. Magn. Magn Mater. 323 (2011) 1954–1962.

[75] R. Mahbub, T. Fakhrul, M.F. Islam, M. Hasan, A. Hussain, M. Matin, M. Hakim, Structural, dielectric, and magnetic properties of Ba-doped multiferroic bismuth ferrite, Acta Metall. Sin. 28 (2015) 958–964.

[76] R. Lebourgeois, J.P. Ganne, B. Lloret, High frequency Mn–Zn power ferrites, J. Phys. IV Fr. 7 (Suppl. C1) (1997) 105–108.

[77] M. Belal Hossen, A.K.M. Akther Hossain, Influence of Al^{3+} substitution on impedance spectroscopy studies of Ni$_{0.27}$Cu$_{0.10}$Zn$_{0.63}$Al$_x$Fe$_{2-x}$O$_4$, Adv. Mater. Lett. 6 (2015) 810–815.

[78] B.C. Das, F. Alam, A.K.M.H. Akther, The crystallographic, magnetic, and electrical properties of Gd^{3+}-substituted Ni–Cu–Zn mixed ferrites, J. Phys. Chem. Solid. 142 (2020), 109433.

[79] J.C. Maxwell, A Treatise on Electricity and Magnetism, Clarendon Press, 1881.

[80] A.S.G. Hassnain Jaffari, A.M. Iqbal, S. Hussain, A. Mumtaz, M.S. Awan, M. Siddique, S.I. Shahd, Effect of A and B-site substitution with Pb, La and Ti on phase stabilization and multiferroic properties of BiFeO$_3$, J. Alloys Compd. 644 (2015) 893–899.

[81] R. Mazumder, A. Sen, Effect of Pb-doping on dielectric properties of BiFeO$_3$ ceramics, J. Alloys Compd. 475 (2009) 577–580.

[82] A.P.B. Selvadurai, V. Pazhanivelu, R. Murugaraj, Strain correlated effect on structural, magnetic, and dielectric properties in Ti^{4+} substituted Bi$_{0.8}$Ba$_{0.2}$Fe$_{1-x}$Ti$_x$O$_3$, Solid State Sci. 46 (2015) 71–79.

[83] A. Dutta, T.P. Sinha, Dielectric relaxation in perovskite BaAl$_{l1/2}$Nb$_{1/2}$O$_3$, J. Phys. Chem. Solid. 67 (2006) 1484–1491.

[84] K.P. Thummer, H.H. Joshi, R.G. Kulkarni, J. Mater. Sci. Lett. 18, 1999, pp. 1529–1532.

[85] B. Tareev, Physics of Dielectric Materials, Mir Publishers, 1979, p. 155.

[86] C. Koops, Phys. Rev. 83, 1953, pp. 121–124.